

Unbiased Image Synthesis via Manifold Guidance in Diffusion Models

Xingzhe Su, Daixi Jia, Fengge Wu, Junsuo Zhao, Changwen Zheng, Wenwen Qiang *

Institute of Software, Chinese Academy of Sciences.

University of Chinese Academy of Sciences.

Beijing, 100190, China

{xingzhe2018, jiadaxi2022, fengge, junsuo, changwen, qiangwenwen}@iscas.ac.cn

arXiv:2307.08199v3 [cs.CV] 15 Apr 2024

Abstract—Diffusion Models are a potent class of generative models capable of producing high-quality images. However, they often inadvertently favor certain data attributes, undermining the diversity of generated images. This issue is starkly apparent in skewed datasets like CelebA, where the initial dataset disproportionately favors females over males by 57.9%, this bias amplified in generated data where female representation outstrips males by 148%. In response, we propose a plug-and-play method named Manifold Guidance Sampling, which is also the first unsupervised method to mitigate bias issue in DDPMs. Leveraging the inherent structure of the data manifold, this method steers the sampling process towards a more uniform distribution, effectively dispersing the clustering of biased data. Without the need for modifying the existing model or additional training, it significantly mitigates data bias and enhances the quality and unbiasedness of the generated images.

Index Terms—Diffusion Models, Image Synthesis, Data Bias, Manifold Guidance

I. INTRODUCTION

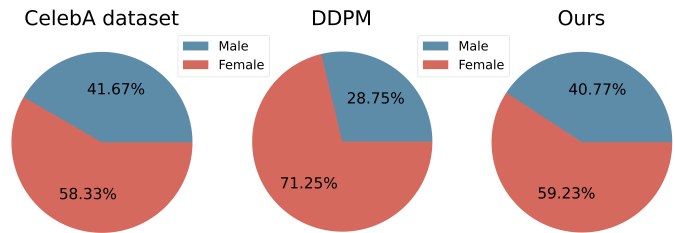
Diffusion Models, also known as Denoising Diffusion Probabilistic Models (DDPMs) [1], stand out as a superior class of generative models, capable of synthesizing high-quality samples from intricate data domains. Surpassing Generative Adversarial Networks (GANs) in various benchmarks [2], they have catalyzed a new wave of applications in image inpainting [3], [4], image super-resolution [5], and 3D point cloud generation [6], [7]. However, despite these significant advancements, DDPMs remain prone to biases inherent in training data, often resulting in skewed and imbalanced outputs [8]–[10].

The manifestation of biases as uneven distributions of data attributes is a growing concern and adversely affects model behavior [11]–[13]. This vulnerability to bias extends to DDPMs. A case in point is the CelebA dataset, widely used in facial recognition tasks, which exhibits gender imbalance that female representation surpasses males by 57.9%. A DDPM trained on this dataset further magnifies this discrepancy, resulting in an output where the proportion of females is 148% higher than that of males, as depicted in Fig.1(b) (middle).

Influenced by biased training data, DDPMs often inherit or exacerbate biases in generated images due to a lack of explicit constraints on the generation distribution. Addressing this issue directly from the data perspective typically necessitates



(a)



(b)

Fig. 1: (a) Images generated by DDPM using standard sampling (left), and manifold-guided sampling (Ours) (right), from the same model. (b) Gender distribution in the CelebA dataset (left), generated data from DDPM using standard sampling (middle), and manifold-guided sampling (Ours) (right).

retraining the DDPMs, incurring substantial computational and time costs [14]. While existing text-to-image generation studies have attempted bias mitigation without retraining [15]–[17], these methods generally depend on prior bias knowledge, which is not readily available preemptively.

To overcome these challenges, we introduce Manifold Guidance Sampling (*MGS*), an innovative unsupervised strategy, leveraging the common assumption that the true data distribution is uniformly spread across its intrinsic manifold [18], [19]. *MGS* modifies the DDPMs' sampling process without additional training, aligning the generated data with the true data manifold. This alignment disrupts the biased clustering of data, leading to a fairer distribution of generated samples and enhanced diversity across image classes, all without the need

* Corresponding author

for prior bias knowledge. To the best of our knowledge, *MGS* is the first unsupervised method designed to systematically counteract bias in DDPMs.

Our method consists of two main components: (1) an unsupervised technique to estimate the true data manifold from training data, designed to disregard the influence of biased samples, and (2) a Manifold Guidance Sampling mechanism to guide the sampling process of DDPMs towards uniform distribution on the estimated manifold. Notably, our method does not require any labels or retraining of the diffusion model, and can be applied to any pre-trained model. We provide theoretical analysis and empirical evidence to show that our method can improve the quality and unbiasedness of samples.

II. PRELIMINARY DDPMs

Let \mathbf{x}_0 be an image, DDPMs firstly construct a forward process $p(\mathbf{x}_{1:N}|\mathbf{x}_0)$ that injects noise to the data distribution $p(\mathbf{x}_0)$. This diffusion process, a type of Markov chain, adheres to $p(\mathbf{x}_t | \mathbf{x}_{t-1}) = \mathcal{N}(\mathbf{x}_t | \sqrt{\alpha_t}\mathbf{x}_{t-1}, \beta_t \mathbf{I})$, where \mathbf{I} is the identity matrix, $\beta_t \in (0, 1)$ is the forward noise schedule, and $\alpha_t := 1 - \beta_t, t = 1, \dots, N$. Utilizing the properties of the conditional Gaussian distribution, the transition probabilities can be expressed as:

$$\begin{aligned} p(\mathbf{x}_t | \mathbf{x}_0) &= \mathcal{N}(\sqrt{\alpha_t}\mathbf{x}_0, (1 - \bar{\alpha}_t) \mathbf{I}) \\ p(\mathbf{x}_{t-1} | \mathbf{x}_t, \mathbf{x}_0) &= \mathcal{N}(\bar{\mu}_t(\mathbf{x}_t, \mathbf{x}_0), \bar{\beta}_t \mathbf{I}) \end{aligned} \quad (1)$$

Here, $\bar{\alpha}_t = \prod_{i=1}^t \alpha_i$, $\bar{\mu}_t = \frac{\sqrt{\alpha_{t-1}}\beta_t}{1-\bar{\alpha}_t}\mathbf{x}_0 + \frac{\sqrt{\alpha_t}(1-\bar{\alpha}_{t-1})}{1-\bar{\alpha}_t}\mathbf{x}_t$ and $\bar{\beta}_t = \frac{1-\bar{\alpha}_{t-1}}{1-\bar{\alpha}_t}\beta_t$.

The reverse process is similarly a Markov chain, designed to approximate $p(\mathbf{x}_0)$ by progressively removing noise, starting from a Gaussian distribution $q(\mathbf{x}_N) = \mathcal{N}(\mathbf{x}_N | 0, \mathbf{I})$:

$$q(\mathbf{x}_{0:N}) = q(\mathbf{x}_N) \prod_{t=1}^N q(\mathbf{x}_{t-1} | \mathbf{x}_t), \quad (2)$$

$$q(\mathbf{x}_{t-1} | \mathbf{x}_t) = \mathcal{N}(\mathbf{x}_{t-1} | \boldsymbol{\mu}_t(\mathbf{x}_t), \bar{\beta}_t \mathbf{I}) \quad (3)$$

$\boldsymbol{\mu}_t(\mathbf{x}_t)$ is generally parameterized by a time-dependent noise estimation model $\epsilon_\theta(\mathbf{x}_t, t)$ [1]. The optimization function is:

$$L_{t-1} = \mathbb{E}_{\mathbf{x}_0, \epsilon} \left[\eta \left\| \epsilon - \epsilon_\theta(\sqrt{\alpha_t}\mathbf{x}_0 + \sqrt{1-\bar{\alpha}_t}\epsilon, t) \right\|^2 \right], \quad (4)$$

where ϵ_θ is an estimation of the noise ϵ , $\eta = \frac{\beta_t^2}{\alpha_t(1-\bar{\alpha}_t)}$ [20].

The diffusion process can also be interpreted as solving a certain stochastic differential equation (SDE) [21]: $d\mathbf{x} = \mathbf{f}(\mathbf{x}, t)dt + g(t)d\mathbf{w}$, where $\mathbf{f}(\mathbf{x}, t)$ and $g(t)$ are diffusion and drift functions of the SDE, and \mathbf{w} is a standard Wiener process. Intriguingly, any diffusion process described by the SDE can be reversed through a corresponding reverse-time SDE:

$$d\mathbf{x} = [\mathbf{f}(\mathbf{x}, t) - g(t)^2 \nabla_{\mathbf{x}} \log p_t(\mathbf{x})] dt + g(t)d\bar{\mathbf{w}} \quad (5)$$

Here $\bar{\mathbf{w}}$ is a standard Wiener process when time flows backwards, and dt denotes an infinitesimal negative time step.

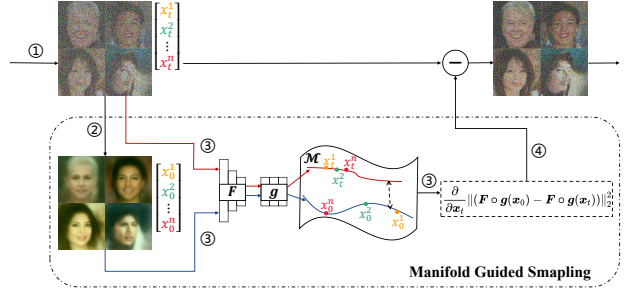


Fig. 2: The sampling process of DDPMs at step t . ① Unconditional reverse diffusion generates $\mathbf{x}_t^i, i = 1, 2, \dots, n$. ② Generate $\hat{\mathbf{x}}_t^i$ from \mathbf{x}_t^i based on Tweedie's formula. ③ Calculate the manifold constraint gradient, where F and g are pre-trained networks. ④ Apply the manifold constraint guidance on the sampling process of DDPMs.

III. METHOD

Without explicit constraints on the generation distribution, DDPMs tend to be influenced by dataset biases and producing data clustered around certain attributes. In response, we propose Manifold Guidance Sampling (*MGS*) which incorporates manifold constraints into the DDPMs' sampling process. This method promotes a uniform distribution of generated samples across the data manifold and effectively disperses biased clustering, all without retraining of the DDPMs. *MGS* unfolds in two phases. First, in **Section III-A**, we propose a novel approach to evaluate the data manifold. Following this, in **Section III-B**, we design a manifold-guided sampling technique in DDPMs. The framework of *MGS* is shown in Fig.2.

A. Data Manifold Evaluation

Evaluating the geometric properties of distributions in high-dimensional ambient space, \mathbb{R}^D , is impractical [22]. In response, we propose mapping high-dimensional data to a low-dimensional space, thereby reducing data complexity and enabling more accurate estimation of the data manifold. Our evaluation emphasizes two steps: learning an efficient mapping to the low-dimensional space and assessing the intrinsic data manifold within the transformed domain.

Step I. Learn an efficient mapping

In this paper, we make a foundational assumption that the true data manifold comprises of low-dimensional nonlinear submanifolds $\cup_{j=1}^k \mathcal{M}_j \subset \mathbb{R}^D$, where each submanifold \mathcal{M}_j has a dimension $d_j \ll D$. This assumption, supported by existing literature [18], posits that images from each submanifold $\mathcal{M}_j \subset \mathbb{R}^D$ can be effectively represented in a lower-dimensional feature space $\mathcal{S}_j \subset \mathbb{R}^d$. Accordingly, in this optimal feature space which mirrors the structure of true data manifold, image representations should exhibit: 1) *Between-Mode Discrepancy*. Representations from different submanifolds should be highly uncorrelated; 2) *Within-Mode Similarity*. Representations from the same submanifold should

be relatively correlated; 3) *Maximally Variance. Representations should have as large dimension as possible to cover all the submanifolds and be variant for the same submanifold.*

1) Objective function. Our objective is to ensure mapped features exhibit the properties above and capture the complex structure of the data manifold. To ensure between-mode discrepancy, features from different submanifolds should span the largest possible volume for a sparse feature distribution. Conversely, features within the same submanifold should span a minimal volume for a compact feature distribution. Thus, we need to measure the relationship between features, focusing on the feature distribution compactness.

Recall that singular values λ_i often correspond to important information implied in a matrix \mathbf{M} . Singular vectors corresponding to larger singular values delineate the principal stretching directions of the data. Specifically, larger and more numerous singular values are characteristic of more uniformly distributed data, while smaller and fewer singular values indicate compactness. Thus, we can use $\mathcal{S} = \sum_{i=1}^k \lambda_i^2$ to measure the compactness of the feature distribution, with larger value of \mathcal{S} indicating a broader span of the singular vectors and thus greater uniformity of the data. Considering computational efficiency, we opt for the trace of $\mathbf{M}\mathbf{M}^T$ instead of \mathcal{S} . Our designed objective function is given by:

$$\mathcal{L}_M(Z) = \frac{1}{2n} \left(\text{Tr}(ZZ^T) - \sum_{j=1}^k \text{Tr}(ZC^jZ^T) \right), \quad (6)$$

where $Z = [z_1, \dots, z_n] \in \mathbb{R}^{d \times n}$ denotes the representations of images, $\mathbf{C} = \{C^j \in \mathbb{R}^{n \times n}\}_{j=1}^k$ is a set of positive diagonal matrices whose diagonal entries denote the membership of the n samples in the k submanifolds. If the sample x_i belongs to the submanifold j , then $C^j(i, i) = 1$. Otherwise, $C^j(i, i) = 0$.

By maximizing the function \mathcal{L}_M , we can enforce compact distribution within submanifolds and uniform distribution across all images, thereby satisfying the required properties. Employing \mathcal{L}_M as the objective function, a convolutional neural network F can be trained as the efficient mapping.

2) Unsupervised learning. In the function \mathcal{L}_M , matrices \mathbf{C} are unknown due to the unavailability of explicit submanifolds. Thus, we provide an unsupervised learning paradigm to infer \mathbf{C} . We utilize a three-layer MLP network g to learn the relationships among samples. The network takes the representations Z , and outputs a matrix $\mathbf{R} \in \mathbb{R}^{n \times n}$, where $\mathbf{R}(i, j)$ denotes the relationship between sample x_i and x_j for $i, j \in \{1, \dots, n\}$. $\mathbf{R}(i, j) = 1$ when x_i and x_j belong to the same submanifold. For each sample x_j , we formulate a diagonal matrix C^j with $C^j(i, i) = \mathbf{R}(j, i)$, thus constructing \mathbf{C} as a set of relationship matrices for each sample.

To facilitate the training of network g , we use a pre-trained encoder E_{pre} to obtain the prior feature representations $\bar{Z} = \{\bar{z}_1, \dots, \bar{z}_n\}$, with $\bar{z}_i = E_{pre}(x_i)$, $i \in \{1, \dots, n\}$. Anchoring on each \bar{z}_i from \bar{Z} , we define a prior relational matrix \mathbf{R}^{pre} using the Gaussian kernel based on the Euclidean distance between the feature representation, modulated by a temperature hyperparameter τ :

$$\mathbf{R}_{i,j}^{pre} = \exp(-\|\bar{z}_i - \bar{z}_j\|_2^2 / \tau) \quad (7)$$

Matrix \mathbf{R}^{pre} serves as a benchmark for the relationships that network g should learn. Thus, we define the loss function for g as the squared Euclidean distance between \mathbf{R}^{pre} and the network's output $g(Z)$ in Eq.8. In the optimal case, g will adeptly learn the underlying relationships between samples, correctly identifying members of the same submanifold.

$$\mathcal{L}_{con} = \|\mathbf{R}^{pre} - g(Z)\|_2^2 \quad (8)$$

3) Training. In our experimental setup, we initiate by training the network g to grasp the intricate relationships between the samples. Then, with the network g fixed, we proceed to train the network F . Finally, we engage in joint training of both F and g using Eq.6 to obtain the optimal mapping F .

Step II. Assess the intrinsic data manifold

Directly computing the data manifold is inherently complex; however, our approach encapsulates the manifold's structure by examining the connections between samples as interpreted by the trained networks F and g . Specifically, we represent data manifold using the matrix $\mathbf{R} = g \circ F(X)$, where \circ denotes the composition of the functions represented by the networks, applying F to input data X followed by g to produce the relational matrix \mathbf{R} . We provide theoretical validation in **Section III-C** that our method accurately captures the data manifold in image space. Further, we offer visualizations of the representations Z and the matrix \mathbf{R} in Appendix C.1. This innovative approach to measuring the data manifold empowers us to enhance the sampling process of diffusion models, ensuring a more representative generation of images.

B. Manifold Guidance Sampling

The central aim of this paper is to facilitate the generation of images uniformly distributed along the true data manifold, denoted as \mathbf{M} . First, we need to estimate \mathbf{M} . According to the Tweedie's formula, for a Gaussian variable $z \sim \mathcal{N}(z; \mu_z, \Sigma_z)$, $\mu_z = z + \Sigma_z \nabla \log p(z)$. From Eq.1, we can get that $\sqrt{\bar{\alpha}_t} \mathbf{x}_0 = \mathbf{x}_t + (1 - \bar{\alpha}_t) \nabla \log p(\mathbf{x}_t)$. Once the score function $\nabla_{\mathbf{x}} \log p_t(\mathbf{x})$ is estimated, we can estimate $\hat{\mathbf{x}}_0$ at every time step. Similarly, once the noise estimation model ϵ_θ is trained, we can get $\hat{\mathbf{x}}_0 = [\mathbf{x}_t - \sqrt{1 - \bar{\alpha}_t} \epsilon_\theta(\mathbf{x}_t, t)] / \sqrt{\bar{\alpha}_t}$. Thus, we can approximate the true data manifold at each time step by a batch of estimated $\hat{\mathbf{x}}_0$, i.e. $\mathbf{M} = \mathbf{H}(\frac{\mathbf{x}_t - \sqrt{1 - \bar{\alpha}_t} \epsilon_\theta(\mathbf{x}_t, t)}{\sqrt{\bar{\alpha}_t}})$, where $\mathbf{H} = g \circ F$ represents the composition of the pre-trained networks from the previous section, \mathbf{x}_t is a batch of samples in our experiments.

Next, we need to add manifold constraint on the sampling process of DDPMs. Based on the Bayes rule $p(\mathbf{x}|\mathbf{M}) = p(\mathbf{M}|\mathbf{x})p(\mathbf{x})/p(\mathbf{M})$, we derive the gradient of the log probability as $\nabla_{\mathbf{x}} \log p(\mathbf{x}|\mathbf{M}) = \nabla_{\mathbf{x}} \log p(\mathbf{x}) + \nabla_{\mathbf{x}} \log p(\mathbf{M}|\mathbf{x})$. To align the generated manifold with the true data manifold, we propose *MGS* that modifies the reverse SDE function (Eq.5) as follows, without necessitating labels or model retraining:

$$d\mathbf{x} = [\mathbf{f}(\mathbf{x}, t) - g(t)^2 \nabla_{\mathbf{x}} \log p_t(\mathbf{x})] dt - \left[\lambda \frac{\partial}{\partial \mathbf{x}} \|\mathbf{M} - \mathbf{H}(\mathbf{x}, t)\|_2^2 \right] dt + g(t) d\bar{\mathbf{w}}. \quad (9)$$

Similarly, we adapt the sampling process of DDPMs to integrate *MGS* into the iterative denoising steps:

$$\mathbf{x}_{t-1} = \frac{1}{\sqrt{\alpha_t}} \left(\mathbf{x}_t - \frac{1 - \alpha_t}{\sqrt{1 - \bar{\alpha}_t}} \boldsymbol{\epsilon}_\theta(\mathbf{x}_t, t) \right) - \lambda \frac{\partial}{\partial \mathbf{x}_t} \|(\mathbf{M} - \mathbf{H}(\mathbf{x}_t))\|_2^2 + \sqrt{\bar{\beta}_t} \mathbf{z}, \quad (10)$$

where \mathbf{M} is the estimated true data manifold, \mathbf{x}_t is a batch of samples, λ is the scale of the manifold guidance. Since diffusion models generate the high-level context in the early stage and fine details in the later stage [23], we apply our method in the early stage to achieve semantic changes.

C. Theoretical Analysis

In this section, we prove that our data manifold evaluation approach can accurately estimate the data manifold in the image space. We begin by establishing the theoretical connection between $\text{Tr}(\mathbf{M}\mathbf{M}^T)$ and information theory. Then, we illustrate the properties of the optimal solution of Eq.6.

Proposition 1: Given finite samples Z from a distribution $P(z)$, and $\mathbf{M} = [z^1, \dots, z^n] \subset \mathbb{R}^{d \times n}$, the square of the Frobenius norm or $\text{Tr}(\mathbf{M}\mathbf{M}^T)$ represents the compactness of this distribution.

The proof of this proposition is available in the Appendix A. In short words, $\text{Tr}(\mathbf{M}\mathbf{M}^T)$ can be seen as a variant to the rate reduction which has been used to measure the ‘‘compactness’’ of a random distribution. Based on this proposition and the data manifold assumption mentioned above, we can infer that the optimal solution of Eq.6 have following properties:

Theorem 1: Suppose \mathbf{Z}^* is the optimal solution that maximizes the objective function Eq.6. We have:

- Between-Mode Discrepancy: If the ambient space is adequately large, the subspaces are all orthogonal to each other, i.e. $(\mathbf{Z}_i^*)^\top \mathbf{Z}_j^* = \mathbf{0}$ for $i \neq j$.

- Maximally Variance: If the coding precision is adequately high, i.e., $\epsilon^4 < \min_j \left\{ \frac{n_j}{n} \frac{d^2}{d_j^2} \right\}$, each subspace achieves its maximal dimension, i.e. $\text{rank}(\mathbf{Z}_j^*) = d_j$.

Therefore, Eq.6 can promote embedding of data into multiple independent subspaces. These properties together ensure that the optimal embedding accurately reflects the data manifold in the feature space, which, in turn, corresponds to the data manifold in the image space. We provide the proof of this theorem in Appendix A.

IV. EXPERIMENTS

We conduct unsupervised generation experiments on six datasets: MNIST [24], Cifar10 [25], CelebA-HQ [26], LSUN-cat, LSUN-bedroom and LSUN-church [27]. We show the quantitative and qualitative results of our method, as well as the comparison with existing methods. The ablation studies of the components in our method are available in Appendix C.2.

A. Experiment Setup

Since our approach is plug-and-play, we can use pre-trained models from DDPM [1]. The generation model for MNIST is finetuned on pre-trained Cifar10 model. We maintain a total of

$N = 1000$ steps with a linear variance schedule and employ three popular schedulers for sampling: DDPM [1], DDIM [20] and PNDM [28], to ensure a comprehensive analysis. Our architecture includes a ResNet-based \mathbf{F} and a three-layer MLP \mathbf{g} . We choose a batch size of 32 for MNIST and Cifar10 datasets, and 16 for other datasets. We opt for SimCLR [29], a self-supervised model [30], [31], as \mathbf{E}_{pre} . Please refer to the Appendix B.2 and C.2 for the rationale for these choices and detailed implementation. To assess the performance of our method, we employ Frechet Inception Distance (FID) [32], the mostly widely-used metric, for evaluating the quality and diversity of the generated images and include sFID [33] to capture the spatial distributional similarity between images.

TABLE I: Comparison of FID \downarrow on four diverse datasets (the red numbers present our improvement)

Datasets	Scheduler	50	100	1000
Cifar10	DDPM	32.72-4.22	9.99-3.12	3.17-0.42
	DDIM	6.99-2.37	5.52-2.24	4.00-1.23
	PNDM	3.95-0.85	3.72-0.92	3.70-0.78
LSUN-church	DDPM	10.84-2.05	10.58-2.37	7.89-1.10
	DDIM	10.0-2.58	9.84-2.05	9.88-1.12
	PNDM	9.89-1.55	10.1-1.19	10.1-1.22
LSUN-bedroom	DDPM	10.81-2.13	6.81-1.66	6.36-1.23
	DDIM	6.05-2.11	5.97-1.54	6.32-1.10
	PNDM	6.44-1.08	6.91-1.12	6.92-0.91
CelebA-HQ	DDIM	8.95-2.20	6.36-1.47	3.41-0.79
	PNDM	3.34-1.03	2.81-0.56	2.86-0.73

B. Experiment Results

First, we focus on the MNIST dataset, characterized by its relative simplicity and balanced distribution of samples across categories. We randomly select a datum and count the number of generated samples (k) that fall within the ϵ -ball neighborhood of this datum, where ϵ represents the average nearest neighbor distance among real samples. This procedure is repeated across 10,000 real samples. If the value of k remains consistent, it strongly suggests a uniform distribution of generated samples on the real data manifold. We perform this experiment on the original DDPM model and our method, with the number of generated samples N ranging from 1,000 to 10,000. The distribution of k is displayed in Fig.3. A uniform distribution of generated samples across the data manifold corresponds to a consistent k value across all real samples, resulting in a Dirac distribution in the histograms presented. It can be observed that our method tends towards such distribution, whereas the baseline model exhibits a heavy-tailed distribution of k . Please refer to Appendix C.1 for additional experiment results.

Next, we conduct a quantitative analysis on the CelebA dataset, which provides 202,599 face images with 40 distinct facial attributes. We focus our bias analysis on three attributes: gender, smile, and beard type. For each attribute, we generate

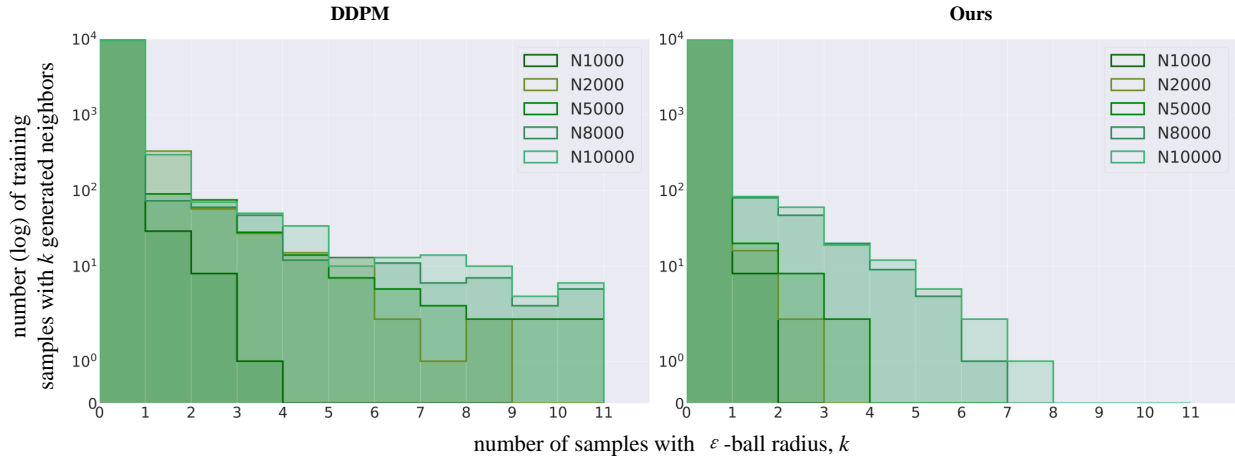


Fig. 3: Distribution of the number of MNIST samples with k generated neighbors within an ε -ball radius. N samples are generated using DDPM model (left) and our method (right). ε is the average nearest neighbor distance for the MNIST samples.

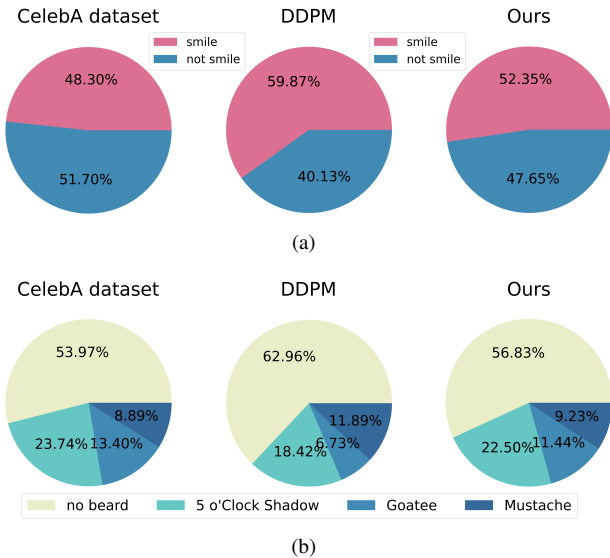


Fig. 4: “Smile” (a) and “Beard” (b) distribution in the CelebA dataset (left), generated data from DDPM using standard sampling (middle), and manifold-guided sampling (right).

12,000 images, classify them using pre-trained models, and calculate the proportions for each category over 10 iterations to average out the results. It can be observed that the original DDPM model significantly favors certain attributes, such as female faces, as demonstrated in Fig.1(b). In the “smile” attribute, with a more uniform distribution in the CelebA dataset (Fig.4(a)), DDPM tends to bias towards smiling faces. Similarly, for beard type (Fig.4(b)), DDPM exhibits noticeable preferences, while our method approaches the distribution of the training dataset more closely. While our method doesn’t achieve completely unbiased generation, it demonstrates effectiveness in addressing bias compared to DDPM. Experiments on other attributes are provided in the Appendix C.1.

Lastly, we evaluate our method using FID metric across

TABLE II: Ablation study on the hyperparameter λ

λ	1	5	10	20
Cifar10	4.62	5.79	7.22	12.3
Church	8.25	7.42	7.97	10.21
Bedroom	5.33	4.69	3.94	7.41
CelebA	7.92	6.75	7.19	10.36

various datasets, time steps, and schedulers, as shown in Table I. The sFID results are available in the Appendix C.1. Notably, the FID scores improve with the application of our method, as indicated by the red numbers in the table. This improvement is consistent across different conditions, showcasing the effectiveness and adaptability of our method. Not requiring model retraining or labels, our approach presents a versatile and effective solution for generating unbiased and diverse images. Visual comparisons between images generated by the original DDPM and our method, highlighting the increased diversity and quality of our generated images, are available in Appendix C.3. These experiments collectively underscore the robustness and broad applicability of our approach.

C. Ablation Study

In this section, we provide ablation and analysis on the hyperparameters. We conduct ablation studies on the hyperparameter λ . We select the pre-trained DDPM model with DDIM scheduler and set the sampling time steps to 50. Table II presents the FID scores of the ablation study conducted on the Cifar10, CelebA-HQ, LSUN-church, and LSUN-bedroom datasets. We empirically set $\lambda = 1$ on Cifar10 dataset, $\lambda = 5$ on CelebA-HQ and LSUN-church datasets, $\lambda = 10$ on LSUN-bedroom dataset.

We also conduct ablation studies on the number of guidance steps. The experiment results on the Cifar10 dataset with 50 sampling time steps are shown in Table III. We apply *MGS* only on the first few sampling steps. It can be seen that different schedulers have different optimal guidance steps. We choose

TABLE III: Ablation study on the Cifar10 dataset

Scheduler	5	10	20	50
DDIM	4.62	5.33	6.42	7.26
PNDM	3.10	3.21	4.03	3.92
DDPM	28.50	29.69	29.77	33.14

the best guidance steps for each scheduler. More experiments on other datasets are available in the Appendix C.2.

V. CONCLUSION

In this work, we focus on addressing the bias issue in diffusion models. We proposed *MGS* to constraint the generated images to be uniformly distributed on the true data manifold. Notably, our method is unsupervised and plug-and-play. This is beneficial since diffusion models have significant computational and energy requirements for training. We provide theoretical and empirical evidence to show the effectiveness and versatility of our method.

ACKNOWLEDGMENT

The authors would like to acknowledge the support and the collaboration effort of the project team. This work was supported by Postdoctoral Fellowship Program of CPSF (GZB20230790), China Postdoctoral Science Foundation (2023M743639), CAS Project for Young Scientists in Basic Research, Grant No. YSBR-040, and Special Research Assistant Fund (E3YD590101), Chinese Academy of Sciences.

REFERENCES

- [1] Jonathan Ho, Ajay Jain, and Pieter Abbeel, “Denoising diffusion probabilistic models,” *Advances in Neural Information Processing Systems*, vol. 33, pp. 6840–6851, 2020.
- [2] Prafulla Dhariwal and Alexander Nichol, “Diffusion models beat gans on image synthesis,” *Advances in neural information processing systems*, vol. 34, pp. 8780–8794, 2021.
- [3] Andreas Lugmayr, Martin Danelljan, Andres Romero, and et al., “Repaint: Inpainting using denoising diffusion probabilistic models,” in *Proceedings of the IEEE/CVF Conference on Computer Vision and Pattern Recognition*, 2022, pp. 11461–11471.
- [4] Hyungjin Chung, Byeongsu Sim, Dohoon Ryu, and et al., “Improving diffusion models for inverse problems using manifold constraints,” 2022, vol. 35, pp. 25683–25696.
- [5] Chitwan Saharia, Jonathan Ho, William Chan, and et al., “Image super-resolution via iterative refinement,” *IEEE Transactions on Pattern Analysis and Machine Intelligence*, 2022.
- [6] Shitong Luo and Wei Hu, “Diffusion probabilistic models for 3d point cloud generation,” in *Proceedings of the IEEE/CVF Conference on Computer Vision and Pattern Recognition*, 2021.
- [7] Alex Nichol, Heewoo Jun, Prafulla Dhariwal, and et al., “Point-e: A system for generating 3d point clouds from complex prompts,” *arXiv preprint arXiv:2212.08751*, 2022.
- [8] Jieyu Zhao, Tianlu Wang, Mark Yatskar, and et al., “Men also like shopping: Reducing gender bias amplification using corpus-level constraints,” in *Proceedings of the 2017 Conference on Empirical Methods in Natural Language Processing*, 2017.
- [9] Tianlu Wang, Jieyu Zhao, Mark Yatskar, and et al., “Balanced datasets are not enough: Estimating and mitigating gender bias in deep image representations,” in *Proceedings of the IEEE/CVF international conference on computer vision*, 2019.
- [10] Melissa Hall, Laurens van der Maaten, Laura Gustafson, and et al., “A systematic study of bias amplification,” *arXiv preprint arXiv:2201.11706*, 2022.
- [11] Benjamin Wilson, Judy Hoffman, and Jamie Morgenstern, “Predictive inequity in object detection,” *arXiv preprint arXiv:1902.11097*, 2019.
- [12] Joy Buolamwini and Timnit Gebru, “Gender shades: Intersectional accuracy disparities in commercial gender classification,” in *Conference on fairness, accountability and transparency*. PMLR, 2018, pp. 77–91.
- [13] Yusuke Hirota, Yuta Nakashima, and Noa Garcia, “Quantifying societal bias amplification in image captioning,” in *Proceedings of the IEEE/CVF Conference on Computer Vision and Pattern Recognition*, 2022, pp. 13450–13459.
- [14] Ling Yang, Zhilong Zhang, Yang Song, Shenda Hong, Runsheng Xu, Yue Zhao, Yingxia Shao, Wentao Zhang, Bin Cui, and Ming-Hsuan Yang, “Diffusion models: A comprehensive survey of methods and applications,” *arXiv preprint arXiv:2209.00796*, 2022.
- [15] Hadas Orgad, Bahjat Kawar, and Yonatan Belinkov, “Editing implicit assumptions in text-to-image diffusion models,” *arXiv preprint arXiv:2303.08084*, 2023.
- [16] Felix Friedrich, Patrick Schramowski, Manuel Brack, Lukas Struppek, Dominik Hintersdorf, Sasha Luccioni, and Kristian Kersting, “Fair diffusion: Instructing text-to-image generation models on fairness,” *arXiv preprint arXiv:2302.10893*, 2023.
- [17] Preethi Seshadri, Sameer Singh, and Yanai Elazar, “The bias amplification paradox in text-to-image generation,” *arXiv preprint arXiv:2308.00755*, 2023.
- [18] Bradley CA Brown, Anthony L Caterini, Brendan Leigh Ross, and et al., “Verifying the union of manifolds hypothesis for image data,” in *The Eleventh International Conference on Learning Representations*, 2022.
- [19] Boxiao Liu, Shenghan Zhang, Guanglu Song, and et al., “Rectifying the data bias in knowledge distillation,” in *Proceedings of the IEEE/CVF International Conference on Computer Vision*, 2021, pp. 1477–1486.
- [20] Jiaming Song, Chenlin Meng, and Stefano Ermon, “Denoising diffusion implicit models,” in *International Conference on Learning Representations*, 2021.
- [21] Yang Song, Jascha Sohl-Dickstein, Diederik P Kingma, and et al., “Score-based generative modeling through stochastic differential equations,” *arXiv preprint arXiv:2011.13456*, 2020.
- [22] Papia Ray, S Surender Reddy, and Tuhina Banerjee, “Various dimension reduction techniques for high dimensional data analysis: a review,” *Artificial Intelligence Review*, vol. 54, pp. 3473–3515, 2021.
- [23] Jooyoung Choi, Jungbeom Lee, Chaehun Shin, and et al., “Perception prioritized training of diffusion models,” in *Proceedings of the IEEE/CVF Conference on Computer Vision and Pattern Recognition*, 2022, pp. 11472–11481.
- [24] Yann LeCun, Léon Bottou, Yoshua Bengio, and et al., “Gradient-based learning applied to document recognition,” *Proceedings of the IEEE*, vol. 86, no. 11, pp. 2278–2324, 1998.
- [25] Alex Krizhevsky, Geoffrey Hinton, et al., “Learning multiple layers of features from tiny images,” 2009.
- [26] Ziwei Liu, Ping Luo, Xiaogang Wang, and Xiaoou Tang, “Deep learning face attributes in the wild,” in *Proceedings of the IEEE international conference on computer vision*, 2015.
- [27] Fisher Yu, Ari Seff, Yinda Zhang, and et al., “Lsun: Construction of a large-scale image dataset using deep learning with humans in the loop,” *arXiv preprint arXiv:1506.03365*, 2015.
- [28] Luping Liu, Yi Ren, Zhijie Lin, and et al., “Pseudo numerical methods for diffusion models on manifolds,” in *International Conference on Learning Representations*, 2022.
- [29] Ting Chen, Simon Kornblith, Mohammad Norouzi, and et al., “A simple framework for contrastive learning of visual representations,” in *International conference on machine learning*. PMLR, 2020, pp. 1597–1607.
- [30] Huijie Guo, Ying Ba, Jie Hu, Lingyu Si, Wenwen Qiang, and Lei Shi, “Self-supervised representation learning with meta comprehensive regularization,” in *Proceedings of the AAAI Conference on Artificial Intelligence*, 2024, vol. 38, pp. 1959–1967.
- [31] Wenwen Qiang, Jiangmeng Li, Changwen Zheng, Bing Su, and Hui Xiong, “Interventional contrastive learning with meta semantic regularizer,” in *International Conference on Machine Learning*. PMLR, 2022, pp. 18018–18030.
- [32] Martin Heusel, Hubert Ramsauer, Thomas Unterthiner, and et al., “Gans trained by a two time-scale update rule converge to a local nash equilibrium,” *Advances in neural information processing systems*, vol. 30, 2017.
- [33] Charlie Nash, Jacob Menick, Sander Dieleman, and et al., “Generating images with sparse representations,” in *International Conference on Machine Learning*. PMLR, 2021.

- [34] Yi Ma, Harm Derksen, Wei Hong, and John Wright, “Segmentation of multivariate mixed data via lossy data coding and compression,” *IEEE transactions on pattern analysis and machine intelligence*, vol. 29, no. 9, pp. 1546–1562, 2007.
- [35] Alec Radford, Jong Wook Kim, Chris Hallacy, and et al., “Learning transferable visual models from natural language supervision,” in *International conference on machine learning*. PMLR, 2021, pp. 8748–8763.
- [36] Kaiming He, Xiangyu Zhang, Shaoqing Ren, and et al., “Deep residual learning for image recognition,” in *Proceedings of the IEEE conference on computer vision and pattern recognition*, 2016, pp. 770–778.
- [37] Yang Song and Stefano Ermon, “Generative modeling by estimating gradients of the data distribution,” *Advances in neural information processing systems*, vol. 32, 2019.
- [38] Yang Song and Stefano Ermon, “Improved techniques for training score-based generative models,” *Advances in neural information processing systems*, vol. 33, pp. 12438–12448, 2020.
- [39] Yang Song, Conor Durkan, Iain Murray, and Stefano Ermon, “Maximum likelihood training of score-based diffusion models,” *Advances in Neural Information Processing Systems*, vol. 34, pp. 1415–1428, 2021.
- [40] Eric Luhman and Troy Luhman, “Knowledge distillation in iterative generative models for improved sampling speed,” *arXiv preprint arXiv:2101.02388*, 2021.
- [41] Robin Rombach, Andreas Blattmann, Dominik Lorenz, and et al., “High-resolution image synthesis with latent diffusion models,” in *Proceedings of the IEEE/CVF Conference on Computer Vision and Pattern Recognition*, 2022, pp. 10684–10695.
- [42] Cheng Lu, Yuhao Zhou, Fan Bao, Jianfei Chen, Chongxuan Li, and Jun Zhu, “Dpm-solver: A fast ode solver for diffusion probabilistic model sampling in around 10 steps,” 2022, vol. 35, pp. 5775–5787.
- [43] Zhaoyang Lyu, Xudong Xu, Ceyuan Yang, Dahua Lin, and Bo Dai, “Accelerating diffusion models via early stop of the diffusion process,” *arXiv preprint arXiv:2205.12524*, 2022.
- [44] Diederik Kingma, Tim Salimans, Ben Poole, and Jonathan Ho, “Variational diffusion models,” *Advances in neural information processing systems*, vol. 34, pp. 21696–21707, 2021.
- [45] Alexander Quinn Nichol and Prafulla Dhariwal, “Improved denoising diffusion probabilistic models,” in *International Conference on Machine Learning*. PMLR, 2021, pp. 8162–8171.
- [46] Cheng Lu, Kaiwen Zheng, Fan Bao, Jianfei Chen, Chongxuan Li, and Jun Zhu, “Maximum likelihood training for score-based diffusion odes by high order denoising score matching,” in *International Conference on Machine Learning*. PMLR, 2022, pp. 14429–14460.
- [47] Minkai Xu, Lantao Yu, Yang Song, Chence Shi, Stefano Ermon, and Jian Tang, “Geodiff: A geometric diffusion model for molecular conformation generation,” in *International Conference on Learning Representations*, 2022.
- [48] Chence Shi, Shitong Luo, Minkai Xu, and Jian Tang, “Learning gradient fields for molecular conformation generation,” in *International Conference on Machine Learning*. PMLR, 2021, pp. 9558–9568.
- [49] Arash Vahdat, Karsten Kreis, and Jan Kautz, “Score-based generative modeling in latent space,” *Advances in Neural Information Processing Systems*, vol. 34, pp. 11287–11302, 2021.
- [50] Valentin De Bortoli, Emile Mathieu, Michael Hutchinson, James Thornton, Yee Whye Teh, and Arnaud Doucet, “Riemannian score-based generative modelling,” 2022, vol. 35, pp. 2406–2422.
- [51] Chin-Wei Huang, Milad Aghajohari, Joey Bose, Prakash Panangaden, and Aaron C Courville, “Riemannian diffusion models,” *Advances in Neural Information Processing Systems*, vol. 35, pp. 2750–2761, 2022.
- [52] Jacob Austin, Daniel D Johnson, Jonathan Ho, Daniel Tarlow, and Rianne van den Berg, “Structured denoising diffusion models in discrete state-spaces,” *Advances in Neural Information Processing Systems*, vol. 34, pp. 17981–17993, 2021.
- [53] Chenlin Meng, Kristy Choi, Jiaming Song, and Stefano Ermon, “Concrete score matching: Generalized score matching for discrete data,” 2022, vol. 35, pp. 34532–34545.
- [54] Xingchao Liu, Lemeng Wu, Mao Ye, et al., “Learning diffusion bridges on constrained domains,” in *The Eleventh International Conference on Learning Representations*, 2023.

The appendix provides additional details and supplementary material to support the main findings and methods presented in this paper. It is organized into several sections: Appendix A provides the proofs of all the theoretical results. Appendix B provides training details for all the experiments that were studied in the main text. Appendix C shows additional results and more visual results that were omitted in the main paper due to page limits. Appendix D introduces the related works and the novelty of our method.

A. Proofs

In this paper, we assume that the true data manifold comprises of a collection of low-dimensional nonlinear submanifolds $\cup_{j=1}^k \mathcal{M}_j \subset \mathbb{R}^D$, where each submanifold \mathcal{M}_j has a dimension $d_j \ll D$. Accordingly, representations of images in the ideal feature space should have following properties: 1) *Between-Mode Discrepancy. Representations from different submanifolds should be highly uncorrelated;* 2) *Within-Mode Similarity. Representations from the same submanifold should be relatively correlated;* 3) *Maximally Variance. Representations should have as large dimension as possible to cover all the submanifolds and be variant for the same submanifold.*

We state our proofs below.

Proposition 2: Given finite samples Z from a distribution $P(z)$, and $\mathbf{M} = [z^1, \dots, z^n] \subset \mathbb{R}^{d \times n}$, the square of the Frobenius norm or $\text{Tr}(\mathbf{M}\mathbf{M}^T)$ represents the compactness of this distribution.

Proof 1: In information theory, there are many methods that can be used to measure the “compactness” of a random distribution such as entropy and rate distortion. Among these methods, rate distortion is a more suitable choice than entropy for continuous random variables with degenerate distributions. Given a random variable z and a prescribed precision $\epsilon > 0$, the rate distortion $R(z, \epsilon)$ is the minimal number of binary bits needed to encode z such that the expected decoding error is less than ϵ . Given finite samples $\mathbf{M} = [z^1, \dots, z^m] \subset \mathbb{R}^{d \times m}$ follow a subspace-like distribution, [34] provides a precise estimate on the number of binary bits needed to encode these samples:

$$\mathcal{R}(\mathbf{M}, \epsilon) \doteq \left(\frac{m+d}{2} \right) \log \det \left(\mathbf{I} + \frac{d}{m\epsilon^2} \mathbf{M}\mathbf{M}^T \right). \quad (11)$$

Based on the first-order Taylor series approximation, $\log \det(\mathbf{C} + \mathbf{D}) \approx \log \det(\mathbf{C}) + \text{Tr}(\mathbf{D}^T \mathbf{C}^{-1})$, we can get:

$$\begin{aligned} & \frac{1}{2n} \text{Tr}(\mathbf{M}\mathbf{M}^T) \\ &= \frac{1}{2} \left(\frac{1}{n} \text{Tr}(\mathbf{M}\mathbf{M}^T) + \log \det(\mathbf{I}) \right) \\ &\approx \frac{1}{2} \log \det \left(\mathbf{I} + \frac{1}{n} \mathbf{M}\mathbf{M}^T \right) \end{aligned}$$

As the sample size m is large, our approach can be seen as an approximation of the rate distortion, which completes our proof.

Theorem 2: Suppose \mathbf{Z}^* is the optimal solution that maximizes the objective function $\mathcal{L}_M(\mathbf{Z}) = \frac{1}{2n}(\text{Tr}(\mathbf{Z}\mathbf{Z}^T) - \text{Tr}(\mathbf{Z}\mathbf{C}\mathbf{Z}^T))$. We have:

- Between-Mode Discrepancy: If the ambient space is adequately large, the subspaces are all orthogonal to each other, i.e. $(\mathbf{Z}_i^*)^\top \mathbf{Z}_j^* = \mathbf{0}$ for $i \neq j$.

- Maximally Variance: If the coding precision is adequately high, i.e., $\epsilon^4 < \min_j \left\{ \frac{n_j}{n} \frac{d^2}{d_j^2} \right\}$, each subspace achieves its maximal dimension, i.e. $\text{rank}(\mathbf{Z}_j^*) = d_j$.

Proof 2: Based on the **Proposition 1**, the objective function \mathcal{L}_M can be rewritten as:

$$\mathcal{L}_M(\mathbf{Z}) \approx \frac{1}{2} \log \det(\mathbf{I} + \alpha \mathbf{Z}\mathbf{Z}^T) - \sum_{j=1}^k \frac{\gamma_j}{2} \log \det(\mathbf{I} + \alpha_j \mathbf{Z}\mathbf{C}^j \mathbf{Z}^T)$$

where $\alpha = \frac{d}{n\epsilon^2}$, $\alpha_j = \frac{d}{\text{tr}(\mathbf{\Pi}^j)\epsilon^2}$, $\gamma_j = \frac{\text{tr}(\mathbf{C}^j)}{n}$ for $j = 1, \dots, k$.

Let $\mathbf{Z}^* = [\mathbf{Z}_1^*, \dots, \mathbf{Z}_k^*]$ be the optimal solution of \mathcal{L}_M .

Suppose that $(\mathbf{Z}_{j_1}^*)^\top \mathbf{Z}_{j_2}^* \neq \mathbf{0}$ for some $1 \leq j_1 < j_2 \leq k$. For the optimal solution \mathbf{Z}^* , there holds a strict inequality function. That is,

$$\mathcal{L}_M(\mathbf{Z}^*) < \sum_{j=1}^k \frac{1}{2n} \log \left(\frac{\det^n \left(\mathbf{I} + \frac{d}{n\epsilon^2} \mathbf{Z}_j^* (\mathbf{Z}_j^*)^\top \right)}{\det^{n_j} \left(\mathbf{I} + \frac{d}{n_j\epsilon^2} \mathbf{Z}_j^* (\mathbf{Z}_j^*)^\top \right)} \right) \quad (12)$$

Since $\sum_{j=1}^k d_j \leq d$, there exists $\{\mathbf{U}'_j \in \mathbb{R}^{d \times d_j}\}_{j=1}^k$ such that the columns of the matrix $[\mathbf{U}'_1, \dots, \mathbf{U}'_k]$ are orthonormal. Denote $\mathbf{Z}'_j = \mathbf{U}'_j \mathbf{\Sigma}_j^* (\mathbf{V}'_j)^T$ the compact SVD of \mathbf{Z}_j^* , and let $\mathbf{Z}' = [\mathbf{Z}'_1, \dots, \mathbf{Z}'_k]$, where $\mathbf{Z}'_j = \mathbf{U}'_j \mathbf{\Sigma}_j^* (\mathbf{V}'_j)^T$.

It follows that:

$$(\mathbf{Z}'_{j_1})^\top \mathbf{Z}'_{j_2} = \mathbf{V}'_{j_1} \mathbf{\Sigma}_{j_1}^* (\mathbf{U}'_{j_1})^\top \mathbf{U}'_{j_2} \mathbf{\Sigma}_{j_2}^* (\mathbf{V}'_{j_2})^\top = \mathbf{V}'_{j_1} \mathbf{\Sigma}_{j_1}^* \mathbf{0} \mathbf{\Sigma}_{j_2}^* (\mathbf{V}'_{j_2})^\top = \mathbf{0} \text{ for all } 1 \leq j_1 < j_2 \leq k.$$

That is, the matrices $\mathbf{Z}'_1, \dots, \mathbf{Z}'_k$ are pairwise orthogonal. For \mathbf{Z}' , we can attain that

$$\begin{aligned} \mathcal{L}_M(\mathbf{Z}') &= \sum_{j=1}^k \frac{1}{2n} \log \left(\frac{\det^n \left(\mathbf{I} + \frac{d}{n\epsilon^2} \mathbf{Z}'_j (\mathbf{Z}'_j)^\top \right)}{\det^{n_j} \left(\mathbf{I} + \frac{d}{n_j\epsilon^2} \mathbf{Z}'_j (\mathbf{Z}'_j)^\top \right)} \right) \\ &= \sum_{j=1}^k \frac{1}{2n} \log \left(\frac{\det^n \left(\mathbf{I} + \frac{d}{n\epsilon^2} \mathbf{Z}_j^* (\mathbf{Z}_j^*)^\top \right)}{\det^{n_j} \left(\mathbf{I} + \frac{d}{n_j\epsilon^2} \mathbf{Z}_j^* (\mathbf{Z}_j^*)^\top \right)} \right) \end{aligned} \quad (13)$$

Comparing Eq.12 and Eq.13 gives $\mathcal{L}_M(\mathbf{Z}') > \mathcal{L}_M(\mathbf{Z}^*)$, which contradicts the optimality of \mathbf{Z}^* . Therefore, we must have $(\mathbf{Z}_{j_1}^*)^\top \mathbf{Z}_{j_2}^* = \mathbf{0}$ for all $1 \leq j_1 < j_2 \leq k$

Moreover, we have

$$\mathcal{L}_M(\mathbf{Z}^*) = \sum_{j=1}^k \frac{1}{2n} \log \left(\frac{\det^n \left(\mathbf{I} + \frac{d}{n\epsilon^2} \mathbf{Z}_j^* (\mathbf{Z}_j^*)^\top \right)}{\det^{n_j} \left(\mathbf{I} + \frac{d}{n_j\epsilon^2} \mathbf{Z}_j^* (\mathbf{Z}_j^*)^\top \right)} \right) \quad (14)$$

We now prove the result concerning the singular values of \mathbf{Z}_j^* . Suppose that there exists $\tilde{\mathbf{Z}}_j$ such that $\|\tilde{\mathbf{Z}}_j\|_F^2 = m_j$, $\text{rank}(\tilde{\mathbf{Z}}_j) \leq d_j$ and

$$\begin{aligned} &\log \left(\frac{\det^n \left(\mathbf{I} + \frac{d}{n\epsilon^2} \tilde{\mathbf{Z}}_j \tilde{\mathbf{Z}}_j^\top \right)}{\det^{n_j} \left(\mathbf{I} + \frac{d}{n_j\epsilon^2} \tilde{\mathbf{Z}}_j \tilde{\mathbf{Z}}_j^\top \right)} \right) \\ &> \log \left(\frac{\det^n \left(\mathbf{I} + \frac{d}{n\epsilon^2} \mathbf{Z}_j^* (\mathbf{Z}_j^*)^\top \right)}{\det^{n_j} \left(\mathbf{I} + \frac{d}{n_j\epsilon^2} \mathbf{Z}_j^* (\mathbf{Z}_j^*)^\top \right)} \right) \end{aligned} \quad (15)$$

Denote $\tilde{\mathbf{Z}}_j = \tilde{\mathbf{U}}_j \tilde{\mathbf{\Sigma}}_j \tilde{\mathbf{V}}_j^\top$ the compact SVD of $\tilde{\mathbf{Z}}_j$ and let $\mathbf{Z}' = [\mathbf{Z}'_1, \dots, \mathbf{Z}'_{j-1}, \mathbf{Z}'_j, \mathbf{Z}'_{j+1}, \dots, \mathbf{Z}'_k]$, where $\mathbf{Z}'_j := \mathbf{U}'_j \tilde{\mathbf{\Sigma}}_j \tilde{\mathbf{V}}_j^\top$.

Note that $\|\mathbf{Z}'_j\|_F^2 = m_j$, $\text{rank}(\mathbf{Z}'_j) \leq d_j$ and $(\mathbf{Z}'_j)^\top \mathbf{Z}'_{j'} = \mathbf{0}$ for all $j' \neq j$. It follows that \mathbf{Z}' is a feasible solution to \mathcal{L}_M and that the components of \mathbf{Z}' are pairwise orthogonal. By using Eq.15, we have

$$\begin{aligned} &\mathcal{L}_M(\mathbf{Z}') \\ &= \frac{1}{2n} \log \left(\frac{\det^n \left(\mathbf{I} + \frac{d}{n\epsilon^2} \mathbf{Z}'_j (\mathbf{Z}'_j)^\top \right)}{\det^{n_j} \left(\mathbf{I} + \frac{d}{n_j\epsilon^2} \mathbf{Z}'_j (\mathbf{Z}'_j)^\top \right)} \right) \\ &\quad + \sum_{j' \neq j} \frac{1}{2n} \log \left(\frac{\det^n \left(\mathbf{I} + \frac{d}{n\epsilon^2} \mathbf{Z}'_{j'} (\mathbf{Z}'_{j'})^\top \right)}{\det^{n_{j'}} \left(\mathbf{I} + \frac{d}{n_{j'}\epsilon^2} \mathbf{Z}'_{j'} (\mathbf{Z}'_{j'})^\top \right)} \right) \\ &= \frac{1}{2n} \log \left(\frac{\det^n \left(\mathbf{I} + \frac{d}{n\epsilon^2} \tilde{\mathbf{Z}}_j (\tilde{\mathbf{Z}}_j)^\top \right)}{\det^{n_j} \left(\mathbf{I} + \frac{d}{n_j\epsilon^2} \tilde{\mathbf{Z}}_j (\tilde{\mathbf{Z}}_j)^\top \right)} \right) \\ &\quad + \sum_{j' \neq j} \frac{1}{2n} \log \left(\frac{\det^n \left(\mathbf{I} + \frac{d}{n\epsilon^2} \mathbf{Z}'_{j'} (\mathbf{Z}'_{j'})^\top \right)}{\det^{n_{j'}} \left(\mathbf{I} + \frac{d}{n_{j'}\epsilon^2} \mathbf{Z}'_{j'} (\mathbf{Z}'_{j'})^\top \right)} \right) \\ &> \frac{1}{2n} \log \left(\frac{\det^n \left(\mathbf{I} + \frac{d}{n\epsilon^2} \mathbf{Z}_j^* (\mathbf{Z}_j^*)^\top \right)}{\det^{n_j} \left(\mathbf{I} + \frac{d}{n_j\epsilon^2} \mathbf{Z}_j^* (\mathbf{Z}_j^*)^\top \right)} \right) \\ &\quad + \sum_{j' \neq j} \frac{1}{2n} \log \left(\frac{\det^n \left(\mathbf{I} + \frac{d}{n\epsilon^2} \mathbf{Z}'_{j'} (\mathbf{Z}'_{j'})^\top \right)}{\det^{n_{j'}} \left(\mathbf{I} + \frac{d}{n_{j'}\epsilon^2} \mathbf{Z}'_{j'} (\mathbf{Z}'_{j'})^\top \right)} \right) \\ &= \sum_{j=1}^k \frac{1}{2n} \log \left(\frac{\det^n \left(\mathbf{I} + \frac{d}{n\epsilon^2} \mathbf{Z}_j^* (\mathbf{Z}_j^*)^\top \right)}{\det^{n_j} \left(\mathbf{I} + \frac{d}{n_j\epsilon^2} \mathbf{Z}_j^* (\mathbf{Z}_j^*)^\top \right)} \right) \end{aligned} \quad (16)$$

Combining it with Eq.14 shows $\mathcal{L}_M(\mathbf{Z}') > \mathcal{L}_M(\mathbf{Z}^*)$, contradicting the optimality of \mathbf{Z}^* . Therefore, the following result holds:

$$\begin{aligned} &\mathbf{Z}_j^* \in \arg \max_{\mathbf{Z}_j} \log \left(\frac{\det^n \left(\mathbf{I} + \frac{d}{n\epsilon^2} \mathbf{Z}_j \mathbf{Z}_j^\top \right)}{\det^{n_j} \left(\mathbf{I} + \frac{d}{n_j\epsilon^2} \mathbf{Z}_j \mathbf{Z}_j^\top \right)} \right) \\ &\text{s.t. } \|\mathbf{Z}_j\|_F^2 = m_j, \text{rank}(\mathbf{Z}_j) \leq d_j \end{aligned} \quad (17)$$

Observe that the optimization problem in Eq.17 depends on \mathbf{Z}_j only through its singular values. That is, by letting $\boldsymbol{\sigma}_j := [\sigma_{1,j}, \dots, \sigma_{\min(m_j, d), j}]$ be the singular values of \mathbf{Z}_j , we have

$$\begin{aligned} & \log \left(\frac{\det^n \left(\mathbf{I} + \frac{d}{n\epsilon^2} \mathbf{Z}_j \mathbf{Z}_j^\top \right)}{\det^{n_j} \left(\mathbf{I} + \frac{d}{n_j \epsilon^2} \mathbf{Z}_j \mathbf{Z}_j^\top \right)} \right) \\ &= \sum_{p=1}^{\min\{n_j, d\}} \log \left(\frac{\left(1 + \frac{d}{n\epsilon^2} \sigma_{p,j}^2\right)^n}{\left(1 + \frac{d}{n_j \epsilon^2} \sigma_{p,j}^2\right)^{n_j}} \right) \end{aligned} \quad (18)$$

also, we have $\|\mathbf{Z}_j\|_F^2 = \sum_{p=1}^{\min\{m_j, d\}} \sigma_{p,j}^2$ and $\text{rank}(\mathbf{Z}_j) = \|\boldsymbol{\sigma}_j\|_0$.

Using these relations, Eq.17 is equivalent to

$$\begin{aligned} & \max_{\boldsymbol{\sigma}_j \in \mathbb{R}_+^{\min\{n_j, d\}}} \sum_{p=1}^{\min\{n_j, d\}} \log \left(\frac{\left(1 + \frac{d}{n\epsilon^2} \sigma_{p,j}^2\right)^n}{\left(1 + \frac{d}{n_j \epsilon^2} \sigma_{p,j}^2\right)^{n_j}} \right) \\ \text{s.t. } & \sum_{p=1}^{\min\{n_j, d\}} \sigma_{p,j}^2 = n_j, \text{ and } \text{rank}(\mathbf{Z}_j) = \|\boldsymbol{\sigma}_j\|_0 \end{aligned} \quad (19)$$

Let $\boldsymbol{\sigma}_j^* = [\sigma_{1,j}^*, \dots, \sigma_{\min\{n_j, d\}, j}^*]$ be an optimal solution to Eq.19. We assume that the entries of $\boldsymbol{\sigma}_j^*$ are sorted in descending order. It follows that $\sigma_{p,j}^* = 0$ for all $p > d_j$ and

$$\begin{aligned} & [\sigma_{1,j}^*, \dots, \sigma_{d_j,j}^*] \\ &= \arg \max_{\substack{[\sigma_{1,j}, \dots, \sigma_{d_j,j}] \in \mathbb{R}_+^{d_j} \\ \sigma_{1,j} \geq \dots \geq \sigma_{d_j,j}}} \sum_{p=1}^{d_j} \log \left(\frac{\left(1 + \frac{d}{n\epsilon^2} \sigma_{p,j}^2\right)^n}{\left(1 + \frac{d}{n_j \epsilon^2} \sigma_{p,j}^2\right)^{n_j}} \right) \\ \text{s.t. } & \sum_{p=1}^{d_j} \sigma_{p,j}^2 = n_j \end{aligned} \quad (20)$$

Then we define

$$f(x; d, \epsilon, n_j, n) = \log \left(\frac{\left(1 + \frac{d}{n\epsilon^2} x\right)^n}{\left(1 + \frac{d}{n_j \epsilon^2} x\right)^{n_j}} \right), \quad (21)$$

and rewrite Eq.20 as

$$\max_{\substack{[x_1, \dots, x_{d_j}] \in \mathbb{R}_+^{d_j} \\ x_1 \geq \dots \geq x_{d_j}}} \sum_{p=1}^{d_j} f(x_p; d, \epsilon, n_j, n) \text{ s.t. } \sum_{p=1}^{d_j} x_p = n_j. \quad (22)$$

We compute the first and second derivative for f with respect to x , which are given by

$$\begin{aligned} f'(x; d, \epsilon, n_j, n) &= \frac{d^2 x (n - n_j)}{(dx + n\epsilon^2)(dx + n_j \epsilon^2)} \\ f''(x; d, \epsilon, n_j, n) &= \frac{d^2 (n - n_j) (nn_j \epsilon^4 - d^2 x^2)}{(dx + n\epsilon^2)^2 (dx + n_j \epsilon^2)^2} \end{aligned} \quad (23)$$

Note that: 1) $0 = f'(0) < f'(x)$ for all $x > 0$; 2) $f'(x)$ is strictly increasing in $[0, x_T]$ and strictly decreasing in $[x_T, \infty)$,

TABLE IV: Ablation study on the Cifar10 dataset

Batch	4	8	16	32	64
FID↓	4.33	4.09	3.28	3.14	3.21

where $x_T = \epsilon^2 \sqrt{\frac{n}{d} \frac{n_j}{d}}$, and 3) by using the condition $\epsilon^4 < \frac{n_j}{n} \frac{d^2}{d_j^2}$, we have $f''\left(\frac{n_j}{d_j}\right) < 0$.

Therefore, we can conclude that the unique optimal solution to Eq.22 is either $\mathbf{x}^* = \left[\frac{n_j}{d_j}, \dots, \frac{n_j}{d_j}\right]$, or $\mathbf{x}^* = [x_H, \dots, x_H, x_L]$ for some $x_H \in \left(\frac{n_j}{d_j}, \frac{n_j}{d_j - 1}\right)$ and $x_L > 0$.

Equivalently, we have either $[\sigma_{1,j}^*, \dots, \sigma_{d_j,j}^*] = \left[\sqrt{\frac{n_j}{d_j}}, \dots, \sqrt{\frac{n_j}{d_j}}\right]$, or $[\sigma_{1,j}^*, \dots, \sigma_{d_j,j}^*] = [\sigma_H, \dots, \sigma_H, \sigma_L]$ for some $\sigma_H \in \left(\sqrt{\frac{n_j}{d_j}}, \sqrt{\frac{n_j}{d_j - 1}}\right)$ and $\sigma_L > 0$, which complete our proof.

B. Experimental Details

1) *Training Setting*: We mainly use ResNet with 4 residual blocks, which have layer widths [64, 128, 256, 512], in our experiments for network \mathbf{F} . We use ResNet18 for MNIST and Cifar10, and ResNet50 for other datasets. We use three-layer MLP for network \mathbf{g} . Across all of our experiments, we use SGD as the optimizer for \mathbf{F} and Adam for \mathbf{g} . We adopt the simple gradient descent–ascent algorithm. We train the models for 800 epochs and use stage-wise learning rate decay every 200 epochs (decay by a factor of 10). We train the models with the full training datasets and on eight NVIDIA RTX A6000 GPUs.

2) *Computation Time*: All our sampling steps are performed with a single NVIDIA RTX A6000 GPU. To generate 4 images of size 256×256 , our method takes about 10 seconds for 25 time steps, 20 seconds for 50 time steps and 300 seconds for 1000 time steps. We conduct ablation study on the batch size of the sampling process. The results are shown in Table IV. In our experiments, given the computational power and time constraints, we have chosen a batch size of 32 for MNIST and Cifar10 datasets, and 16 for other datasets.

C. Additional Experimental Results

1) *Additional Results*: We conduct the same experiment as Fig.3 on the MNIST dataset, with 0.8ϵ -ball radius and 1.2ϵ -ball radius. The experiment results are shown in Fig.5 and Fig.6.

For the quantitative experiment on the CelebA dataset, we also conduct experiments on the attributes: hair color, hair style, bangs type and young. The results are shown in Fig.7. The DDPM still exhibits noticeable preferences, while our method approaches the distribution of the training dataset more closely. While our method doesn't achieve completely unbiased generation, it demonstrates effectiveness in addressing bias compared to DDPM.

The comparison of FID and sFID scores is shown in Table V and Table VI. In general, the sFID scores of our method show a significant and consistent advantage over all the compared methods.

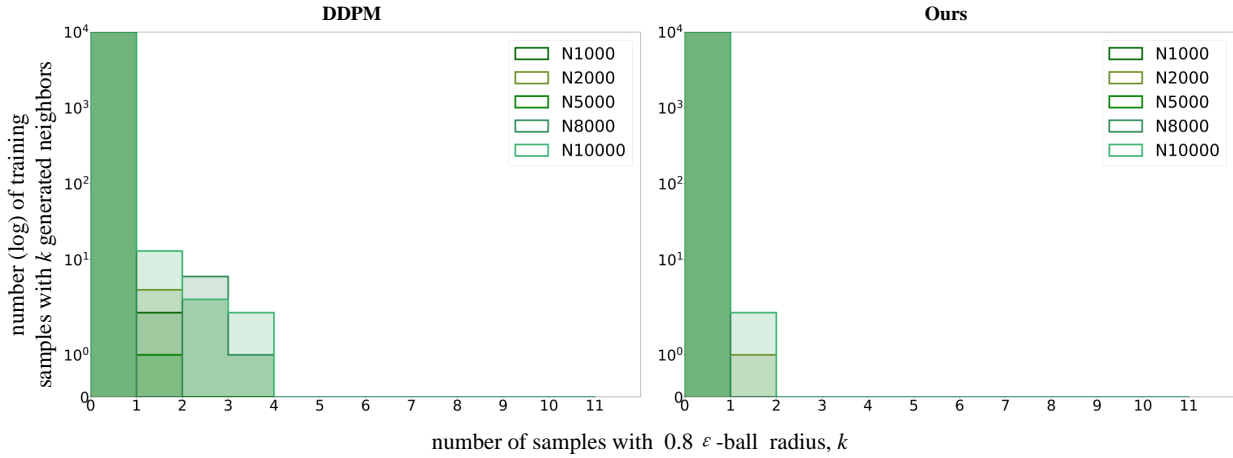


Fig. 5: Distribution of the number of MNIST training samples with k neighbors generated within a 0.8ε -ball radius. Left shows the results of DDPM. Right shows the results of our method.

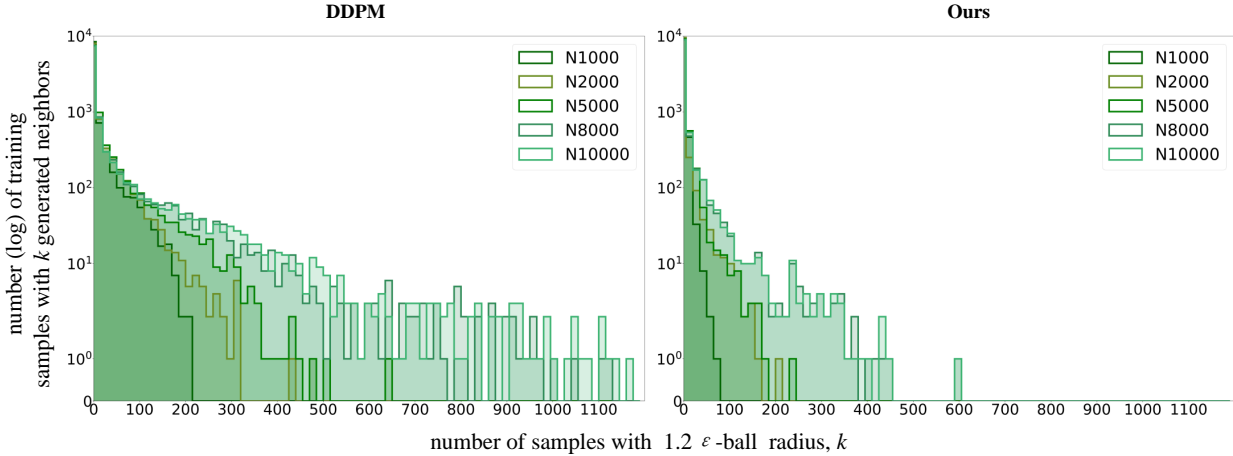


Fig. 6: Distribution of the number of MNIST training samples with k neighbors generated within a 1.2ε -ball radius. Left shows the results of DDPM. Right shows the results of our method.

We present visualizations of the representations learned by the network F for Cifar10 in Fig.8(a). We also visualize the \mathbf{R} matrix for 100 randomly selected samples from the Cifar10 dataset in Fig.8(b). Moreover, we provide visualizations of the generated image representations. The images are generated by the original DDPM model (Fig.8(c)) and our method (Fig.8(d)), respectively. These representations are extracted using a classifier trained on the Cifar10 dataset. Notably, the network F is capable of acquiring refined representations, with the \mathbf{R} matrix closely resembling the ground truth. Furthermore, our method outperforms the original DDPM model, yielding more uniformly generated images.

2) *Ablation Study*: In this section, we provide ablation and analysis over different components of our method.

Relationship Matrices \mathbf{C} . We offer several implementation methods for obtaining the relationship matrices \mathbf{C} in \mathcal{L}_M . The first approach utilizes the contrastive learning model SimCLR [29] in combination with K-means clustering. We employ a pre-trained SimCLR model to extract features from the training

dataset, and then perform K-means clustering on these features. The resulting clustering centroids serve as prototypes of the submanifolds. In this experiment, we consider using 10 and 20 clustering centroids as options. The second approach introduces learnable matrices, which is proposed in this paper. We choose the pre-trained encoders E_{pre} to be SimCLR, CLIP [35], and ResNet50 [36] (pre-trained on the ImageNet). We use the DDPM model with DDIM scheduler for experiments and set the sampling time steps to 50. Table VII presents the FID scores of the ablation study conducted on the Cifar10, CelebA-HQ, LSUN-church, and LSUN-bedroom datasets. It can be observed that the choice of the pre-trained encoder has minimal impact on the results. For our subsequent experiments, we opt for the learnable approach using the SimCLR model as the pre-trained encoder.

Hyperparameters. We also conduct ablation studies on the number of guidance steps. The experiment results on the LSUN-church, LSUN-bedroom, CelebA-HQ datasets with 50 sampling time steps are shown in Table VIII, Table IX and

TABLE V: Comparison of FID \downarrow on four diverse datasets (the red numbers present our improvement)

Datasets	Scheduler	20	50	100	1000
Cifar10	DDPM	133.37- 5.32	32.72- 4.22	9.99- 3.12	3.17- 0.42
	DDIM	10.9- 2.85	6.99- 2.37	5.52- 2.24	4.00- 1.23
	PNDM	5.00- 1.23	3.95- 0.85	3.72- 0.92	3.70- 0.78
LSUN-church	DDPM	12.47- 3.14	10.84- 2.05	10.58- 2.37	7.89- 1.10
	DDIM	11.7- 2.89	10.0- 2.58	9.84- 2.05	9.88- 1.12
	PNDM	9.13- 1.24	9.89- 1.55	10.1- 1.19	10.1- 1.22
LSUN-bedroom	DDPM	22.77- 4.13	10.81- 2.13	6.81- 1.66	6.36- 1.23
	DDIM	8.47- 1.97	6.05- 2.11	5.97- 1.54	6.32- 1.10
	PNDM	5.68- 1.24	6.44- 1.08	6.91- 1.12	6.92- 0.91
CelebA-HQ	DDIM	13.4- 2.75	8.95- 2.20	6.36- 1.47	3.41- 0.79
	PNDM	5.51- 1.11	3.34- 1.03	2.81- 0.56	2.86- 0.73

TABLE VI: Comparison of sFID \downarrow on the four diverse Datasets (the red numbers present our improvement)

Datasets	Scheduler	20	50	100	1000
Cifar10	DDPM	80.34- 10.79	40.18- 8.44	12.23- 5.03	5.74- 0.89
	DDIM	21.00- 5.78	11.31- 5.28	9.88- 4.96	6.18- 2.04
	PNDM	8.31- 2.45	6.70- 1.76	6.53- 1.47	6.50- 1.23
LSUN-church	DDPM	24.19- 7.26	23.9- 4.23	21.52- 5.56	11.25- 2.07
	DDIM	22.69- 4.97	22.13- 5.39	18.23- 3.8	18.35- 1.93
	PNDM	18.03- 2.31	18.25- 2.73	22.67- 1.93	22.66- 1.94
LSUN-bedroom	DDPM	35.72- 8.29	23.84- 4.34	11.31- 4.28	11.07- 2.04
	DDIM	15.86- 3.27	10.73- 3.04	10.35- 2.67	10.97- 1.78
	PNDM	10.12- 2.43	11.20- 2.29	11.79- 1.86	11.80- 1.16
CelebA-HQ	DDIM	26.09- 4.69	13.22- 4.14	11.23- 3.23	5.63- 1.42
	PNDM	9.82- 1.78	5.53- 1.49	4.69- 1.04	4.73- 1.55

TABLE VII: Ablation study on the relationship matrices C

Method	Cifar10	Church	Bedroom	CelebA
Baseline	6.99	10.0	6.05	8.95
K-means(10)	6.28	8.26	4.73	7.26
K-means(20)	6.49	8.79	5.24	7.22
learnable (SimCLR)	4.62	7.42	3.94	6.75
learnable (CLIP)	4.74	7.73	4.16	6.77
learnable (ResNet)	4.92	7.33	3.82	6.89

TABLE VIII: Ablation study on the LSUN-church dataset

Guidance steps	5	10	20	50
DDIM	7.42	7.57	8.46	9.24
PNDM	8.61	8.34	9.23	9.82
DDPM	9.25	8.79	9.73	10.14

Table X. We apply *MGS* only on the first few sampling steps. It can be seen that different schedulers have different optimal guidance steps. We choose the best guidance steps for each scheduler.

TABLE IX: Ablation study on the LSUN-bedroom dataset

Scheduler	5	10	20	50
DDIM	3.94	4.13	4.87	5.18
PNDM	5.67	5.36	6.22	6.36
DDPM	8.03	7.68	8.45	9.79

TABLE X: Ablation study on the CelebA-HQ dataset

Scheduler	5	10	20	50
DDIM	6.75	6.83	7.25	7.92
PNDM	2.76	2.31	3.22	3.43

3) *Visual Results*: The visual results of different datasets are shown in Fig.9, Fig.10, Fig.11 and Fig.12, respectively. Our method outperforms DDPM on image diversity and quality.

D. Related Works

Diffusion models are a family of probabilistic generative models that can produce high-quality samples from complex data domains. There are three main formulations of diffusion models: denoising diffusion probabilistic models (DDPMs) [1], [20], score-based generative models (SGMs) [37], [38], and stochastic differential equations (Score SDEs) [21], [39]. A major challenge of diffusion models is their slow and costly

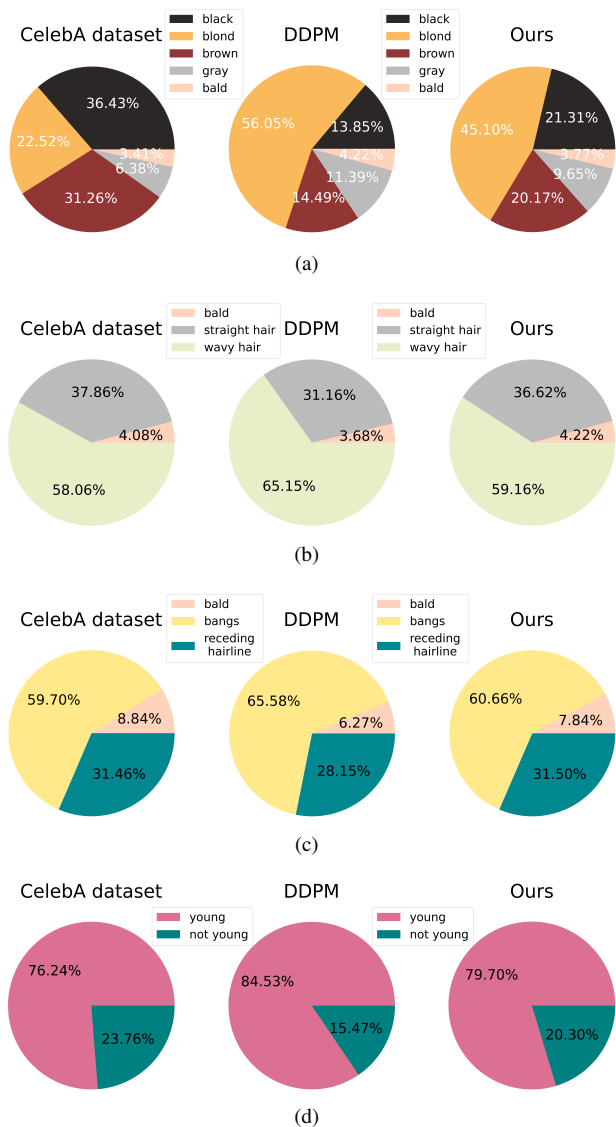


Fig. 7: “Hair Color” (a), “Hair Style” (b), “Bangs Type” (c) and “Young” (d) distributions in the CelebA dataset (left), generated data from DDPM using standard sampling (middle), and manifold-guided sampling (right)

sampling process [14], which has motivated several research directions to improve their efficiency and accuracy [20], [28], [40]–[46]. Another research direction is to adapt diffusion models to data with special structures or properties, such as permutation invariance [47], [48], manifold structures [49]–[51], and discrete data [52]–[54].

In this paper, we address a critical yet overlooked issue in current research: the bias issue in generated samples. A recurring phenomenon in the outputs of DDPMs is the propensity for these samples to aggregate around particular modes of the training data, thereby engendering a non-uniform distribution across the data manifold. Furthermore, most diffusion models are trained on web-scraped image datasets, which may contain implicit or explicit biases that reflect the

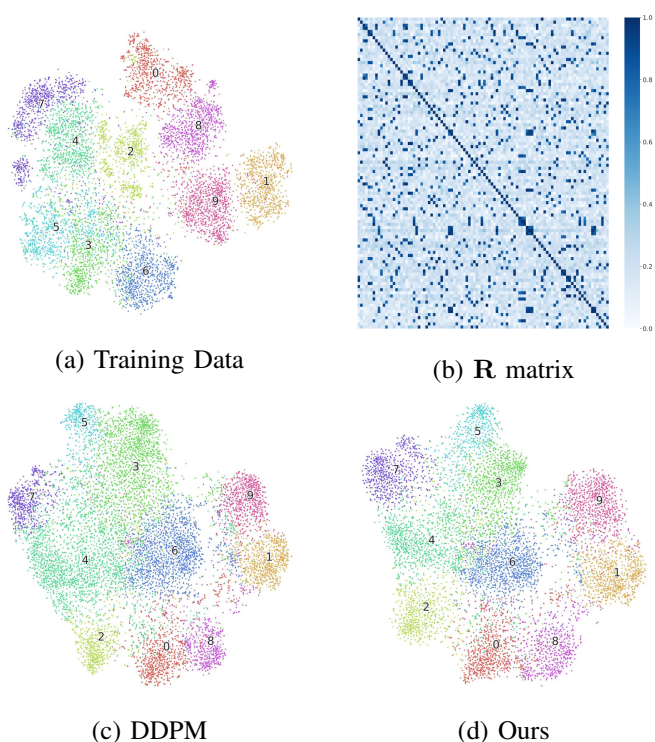


Fig. 8: (a) Visualization of the representations learned by the network F for Cifar10 dataset. (b) Visualization of the \mathbf{R} matrix. (c) and (d) Representations of images generated by DDPM model and our method.

skewed or imbalanced patterns of the data collection process. Such biases can adversely affect the quality and diversity of the generated samples, as well as downstream tasks that rely on them. Previous works [15]–[17] also identify a similar issue with text-to-image diffusion models, and propose a method to edit implicit assumptions in the pre-trained models. However, their methods require prior knowledge of attributes the data exhibit bias in. Acquiring such priors can be challenging, whereas our method does not rely on this prior. Moreover, the authors in [4] propose to add manifold constraint guidance on conditional diffusion models. Their method relies on predefined prompts and focuses more on inverse problems, whereas our method is unsupervised and aims to alleviate data bias problem of image generation. PNDM [28] proposes a pseudo numerical method to generate sample along a specific manifold in \mathcal{R}^N . This method aims to reduce the noise introduced by numerical methods and the manifold is defined by a single sample, whereas our method estimates the manifold based on training data and aims to reduce the data bias in sampling.



Fig. 9: Random batch of samples generated from DDPM (left) and MGS (right) on the CelebA-HQ dataset. Samples are sorted and color coded by gender.



Fig. 10: Random batch of samples generated from DDPM (left) and *MGS* (right) on the LSUN-cat dataset.



Fig. 11: Random batch of samples generated from DDPM (**left**) and *MGS* (**right**) on the LSUN-church dataset.



Fig. 12: Random batch of samples generated from DDPM (left) and *MGS* (right) on the LSUN-bedroom dataset.